Metals

CrossMark

Microstructure and corrosion characterization of the nugget region in dissimilar friction-stir-welded AA5083 and AA1050

A. Fattah-alhosseini[1], M. Naseri[2,*] (iD), D. Gholami[3], O. Imantalab[1], F. R. Attarzadeh[4], and M. K. Keshavarz[5]

[1] *Department of Materials Engineering, Bu-Ali Sina University, Hamedan 65178-38695, Iran*

[2] *Department of Materials Science and Engineering, Faculty of Engineering, Shahid Chamran University of Ahvaz, Ahvaz, Iran*

[3] *School of Metallurgy and Materials Engineering, Iran University of Science and Technology (IUST), Tehran, Iran*

[4] *Department of Chemical Engineering, University of Arkansas, Fayetteville, AR, USA*

[5] *Department of Mining and Materials Engineering, McGill University, Montreal, QC H3A 0C5, Canada*

ABSTRACT

Metallurgical structure, mechanical properties and electrochemical behavior of dissimilar friction stir welding (FSW) between structural AA5083 and AA1050 alloys were investigated in this study. Optical microscopy and field emission scanning electron microscopy observations showed that the nugget zone (NZ) possesses equiaxed recrystallized grains of the two alloys with a flowing shape. Energy-dispersive spectroscopy analysis revealed that NZ is mainly composed of the advancing side alloy. The ultimate tensile and yield strengths of the dissimilar FSW joint were higher than those of AA1050 and lower than those of AA5083. Consequently, fracture occurred on AA1050 side during the tensile tests. The potentiodynamic polarization (PDP) results revealed that the passive current density of the FSW joint was in between that of AA1050 and AA5083. A modified Randles equivalent circuit was used to simulate the obtained experimental data of electrochemical impedance spectroscopy measurements. The acquired impedance parameters were in good agreement with the PDP measurements.

Introduction

Joining dissimilar materials is often an essential part of manufacturing industries where complex loading conditions exist. This need demands the availability of comprehensive joining methods of dissimilar materials in order to design lightweight and high-performance complex structures. Aluminum alloys have been widely used in engineering structures owing to their high electric and heat conductivities, corrosion resistance and mechanical properties. For these reasons, they have been extensively employed in aerospace, automotive and marine applications.

Address correspondence to E-mail: majid_na3ri@yahoo.com; m-naseri@phdstu.scu.ac.ir

Springer

This family of alloys has low weldability with conventional fusion welding techniques [1–3].

Friction stir welding (FSW) dates back to 1991, when The Welding Institute (TWI) located in Cambridge, UK, introduced this novel solid-state joining technique for the first time [4, 5]. This technique involves a non-consumable cylindrical tool harnessed with a specially designed pin and shoulder, rotating at a very high speed and plunging into adjacent edges of the metal pieces, in which a suitable weld joint forms between the work pieces. In this process, the welding starts with bringing the work pieces into contact and proceeds with the frictional heating of the rotating tool that is pressed at their interface, transforming the interfacial region into a plasticized state. During the translation of the tool along the joint line, the tool stirs and forges the material from its front face to its trailing face where it finally cools down and turns into a solid-state weld. During this solid-state welding process, problems such as liquation cracking, porosity formation and distortion common in other welding processes are not expected. Since the process does not require any filler metal in contrast to fusion welding, the compatibility of composition between the filler metal and parent materials is not a challenge in FSW processes [6, 7].

Generally, four distinct zones appear in FSW-processed aluminum alloys and each of them has certain characteristics: (1) the thermomechanically affected zone (TMAZ), (2) the heat-affected zone (HAZ), (3) the stir zone (SZ) and (4) the base material (BM). TMAZ is created by plastic deformation of parent materials during the welding process, and HAZ owes its formation to weld thermal cycle. On the other hand, SZ formation is due to recrystallization caused by severe plastic deformation, and BM is where the material is not affected by welding at all. TMAZ has a partially recrystallized fine-grained microstructure that owes it formation to the concurrency of extremely high plastic deformation and elevated temperatures. This region is commonly called the nugget zone (NZ) [8–10]. Hence, aluminum alloys experience significant microstructural evolution during FSW processes. Subsequently, these processes will have significant impacts on the microstructure, mechanical properties and electrochemical behavior.

There seems to exist some contradictions in studying the effect of FSW parameters on different properties of resulted joints for various alloys. Thus, optimization of the process parameters is of paramount importance to obtain suitable FSW joints. In a study conducted on 2219Al-T651 alloy, Babu and colleagues found that inferior mechanical properties are to be expected from the FSW process when it involves high rotation rates or low welding speeds [11]. On the contrary, Zhang et al. reported that FSW of the same alloy at high welding speeds enhanced the tensile strength and it was less dependent on the rotation rate [12]. Moreover, Liu et al. [13] and Zhou et al. [14, 15] studied the effects of FSW on Ti–6Al–4V plates and found that the SZ microstructure exhibited a mixture of the equiaxed grains and lamellar structure. Both groups pointed out that lowering the heat input gave rise to improved mechanical properties. In addition, the microstructural evolution and electrochemical corrosion behavior of dissimilar FSW joints between AA5083 and AA6082 were comparatively investigated by Shen et al. [16]. They concluded that the corrosion resistance of SZ was superior to those observed in the parent alloys at any given welding condition. On the other hand, Park et al. studied the evolution of mechanical properties in a localized fashion after joining AA5052-H32 and AA6061-T6 alloys via FSW [17]. They showed that positioning the softer AA5052-H32 on the advancing side eventuated in an advancing side that had low hardness values and the same side underwent tensile fracture.

However, to study and understand the electrochemical behavior of dissimilar FSW joint, it is crucial to analyze its microstructure within the various affected regions. Although pure Al oxide film is expected to be stable within the pH range of about 4–8, little is known about corrosion and passive behavior of FSW-processed aluminum alloys in alkaline media. The present research work, to the best of our knowledge, is the first of its kind that discusses how FSW influences microstructural evolution, mechanical properties and electrochemical behavior of dissimilar AA5083 and AA1050 alloy joints in borate buffer solutions of different pH values (7.0, 8.2 and 8.9).

Experimental procedure

Materials and FSW process

In this work, 5-mm-thick plates of AA1050 and AA5083 with a surface area of 120 mm by 60 mm were used. The nominal chemical compositions of

these alloys are given in Table 1. The FSW process was carried out using a TOS FGU 32 milling machine, where the stronger AA5083 was positioned on the advancing side (AS) and AA1050 alloy on the retreating side (RS). This configuration was adopted to obtain a stronger joint (Fig. 1). The stir welding tool had a pin with 6 mm diameter and 5.7 mm length accompanied by a shoulder of 18 mm diameter. As for the processing parameters, tool rotation speed and welding speed were maintained at 1000 rpm and 40 mm/min, respectively.

Microstructural evaluation

Microstructural evaluations were performed by an optical microscope (OM) and a field emission scanning electron microscope (FESEM, VEGA\\-TESCAN) equipped with an energy-dispersive spectroscopy (EDS). The studied surfaces were on the weld cross sections and perpendicular to the welding direction. The preparation of samples was followed by grinding and polishing according to common metallographic procedures to obtain mirror surfaces. They were eventually etched in a solution of 10 ml perchloric acid and 90 ml alcohol for 8 s. AA1050 and AA5083 parent materials were electrochemically etched in a 2% fluoroborate solution and an electrolyte composed of mixed acids (1 ml HF: 1.5 ml HCl: 2.5 ml HNO_3: 95 ml H_2O), respectively.

Mechanical properties

Vickers microhardness measurements were taken on the cross sections of the welds along a line at the half thickness of plates using a programmable Buehler hardness tester applying 100 g force for 10 s. The specimens for transverse tensile tests with a gage length of 25 ± 0.1 mm and a gage width of
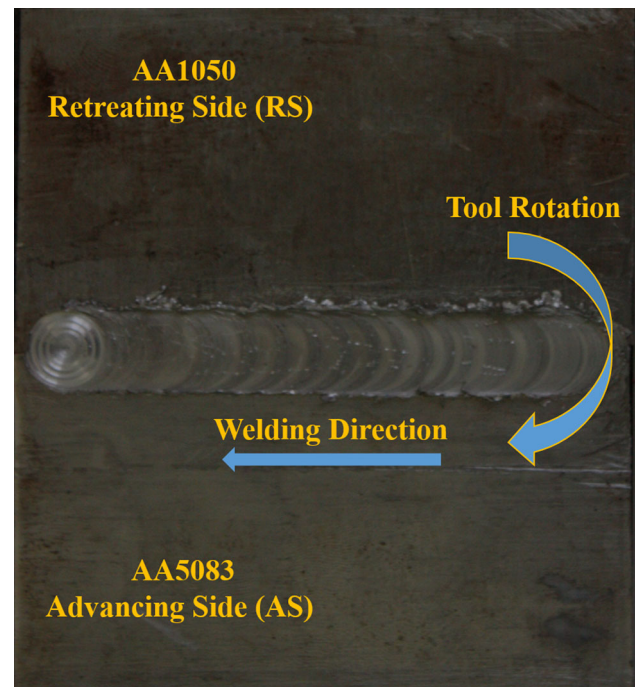
Figure 1 Picture of dissimilar friction-stir-welded joint.

6 ± 0.1 mm were machined perpendicular to the FSW direction according to the ASTM: E8 M. The tensile tests were carried out at the ambient temperature and a strain rate of 1.67×10^{-4} s^{-1} using a SANTAM STM-50 tensile testing instrument. These tests were repeated three times at any given FSW condition. The fracture surfaces of the tensile specimens were also studied by FESEM.

Electrochemical measurements

A µAutolab Type III/FRA2 system was used for the electrochemical impedance spectroscopy (EIS) and the potentiodynamic polarization to investigate the passive behavior of the FSW-processed specimens.

Table 1 Chemical composition (wt%) of used AA1050 and AA5083 plates

Fe	Si	Cu	Ti	Zn	Ni	Al		
AA1050								
0.352	0.027	0.020	0.020	0.016	< 0.005	Rest		
Cu	Mg	Si	Fe	Mn	Zn	Ti	Cr	Al
AA5083								
0.062	4.510	0.219	0.400	0.400	0.060	0.043	0.107	Rest

Figure 2 Optical micrograph of cross sections perpendicular to the tool traverse direction of the dissimilar FSW joint.
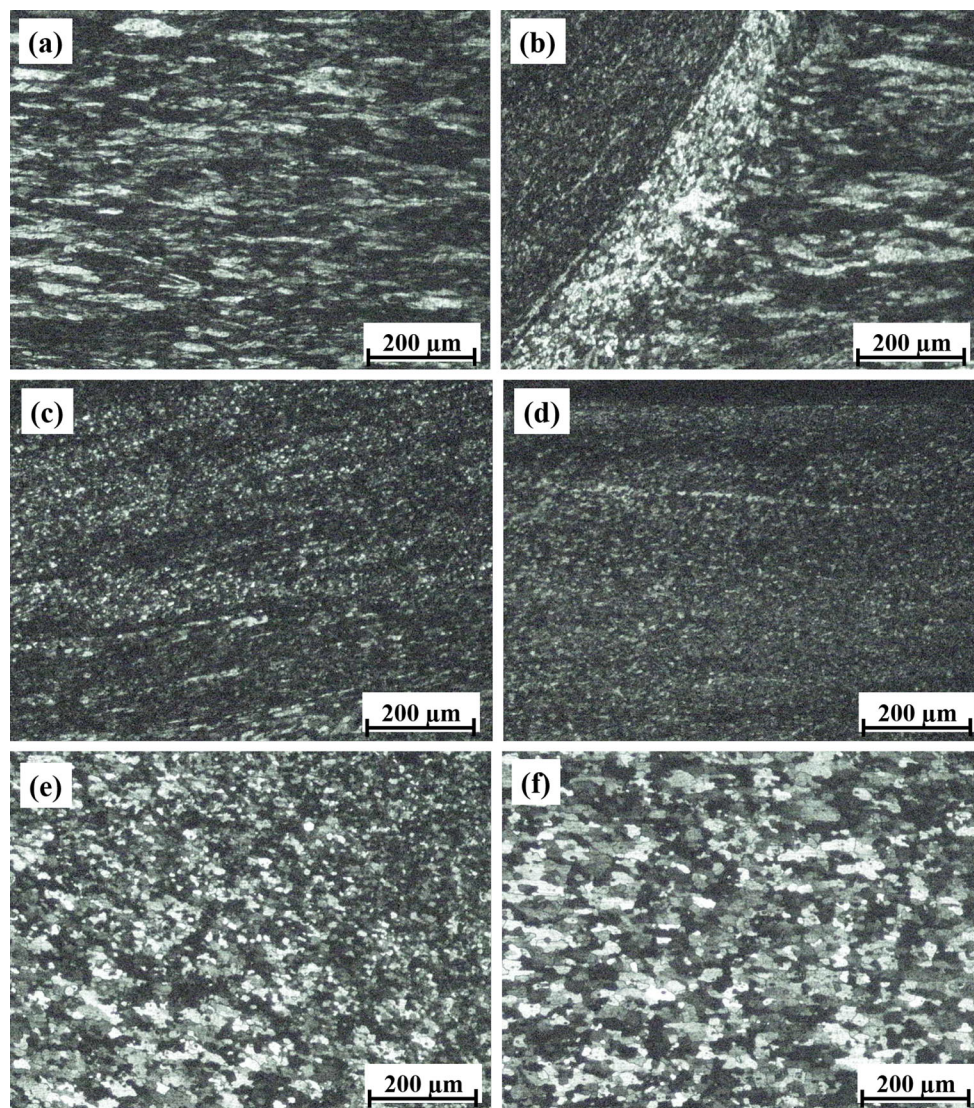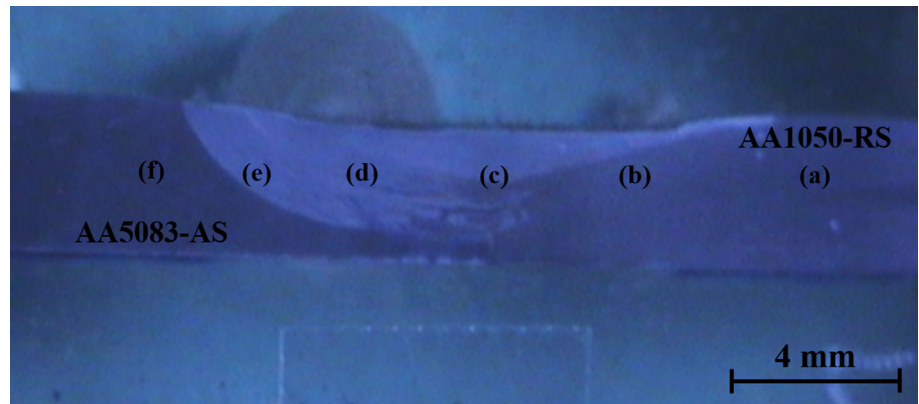

Figure 3 Optical micrographs of welding regions AA1050 side (**a**–**c**) and AA5083 side (**d**–**f**).

The sample preparation procedures for these analyses include grinding the sample surfaces to 5000 grit and washing by deionized water. The electrochemical measurement cell was a standard three-electrode

Figure 4 a SEM micrograph and EDS analysis of dissimilar FSW joint and **b** higher magnification of selected area.

	Wt%	σ
Al	58.0	0.6
Fe	23.8	0.5
Mn	9.3	0.4
C	4.6	0.5
Si	3.1	0.2
Cr	1.2	0.2
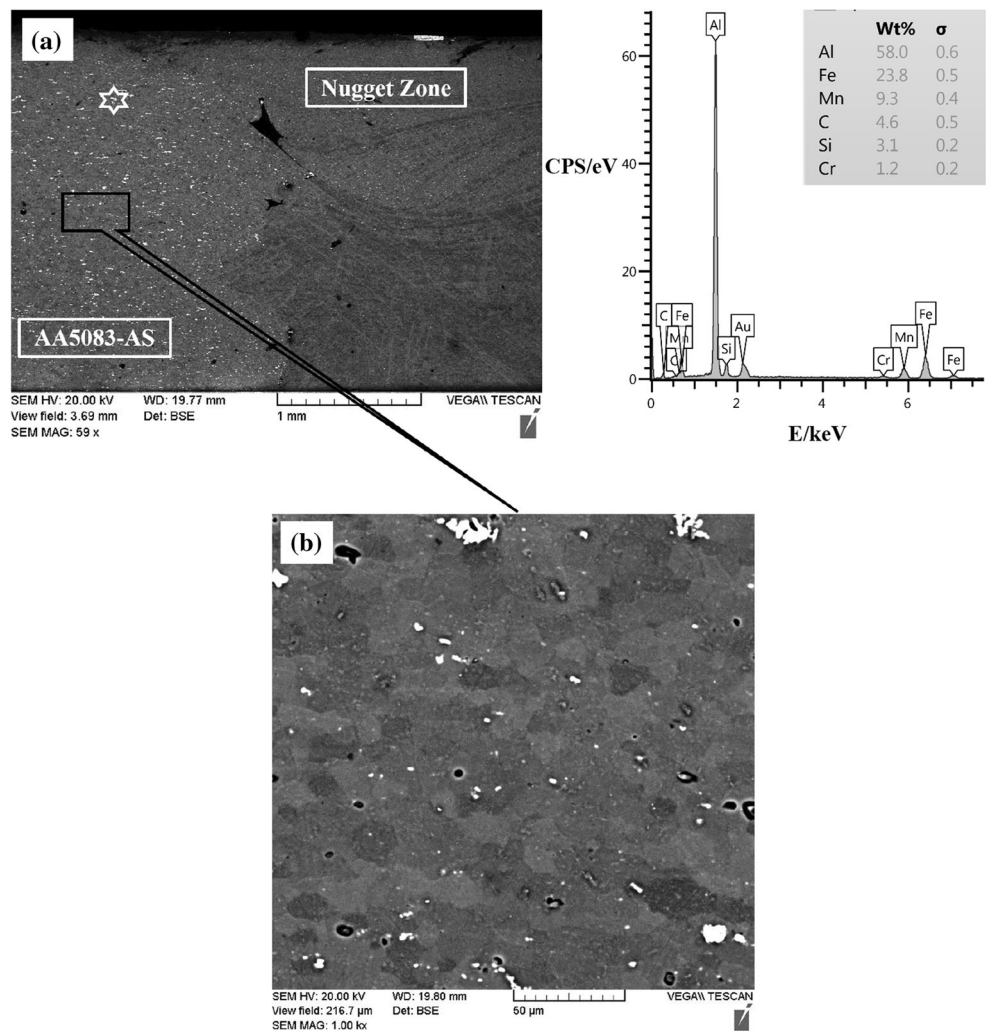
setup with the samples acquired from different weld regions as the working electrode (AA1050, SZ and AA5083 regions), an Ag/AgCl saturated in KCl as the reference electrode and a Pt plate as the counter electrode. The measurements were taken at room temperature in borate buffer solutions of different pH values (7.0, 8.2 and 8.9). The polarization curves were obtained in a potential range starting from -250 mV with respect to the open circuit potential (OCP) and ending at $+1000$ mV with respect to the reference electrode using a scan rate of 1 mV/s. Prior to these measurements, OCP was monitored for 2 h and the system was allowed to reach a steady-state condition. An AC perturbation of ± 10 mV and a frequency range of 100 kHz to 10 mHz were considered for the execution of EIS tests. The EIS data were fitted and an equivalent circuit (EC) was proposed using NOVA impedance software. The reproducibility of

electrochemical analysis was also confirmed by repeating each test at least four times.

Results and discussion

Microstructural observations

The macrostructure of the FSW-processed joint is shown in Fig. 2. Also, the microstructures of different zones on the joint are shown in Fig. 3. The advancing (AS) and retreating (RS) sides are on the left and right sides of the weld, respectively. The absence of macroscopic defects such as voids, cracks or discontinuities in SZ means that FSW was successful in joining these dissimilar alloys. In addition, a basin-shaped SZ is evident at the center of the FSW joint, which is extended from the bottom to the top surface of the sheet because of the friction induced between

Figure 5 Microhardness distribution of dissimilar FSW cross section performed at the midthickness.
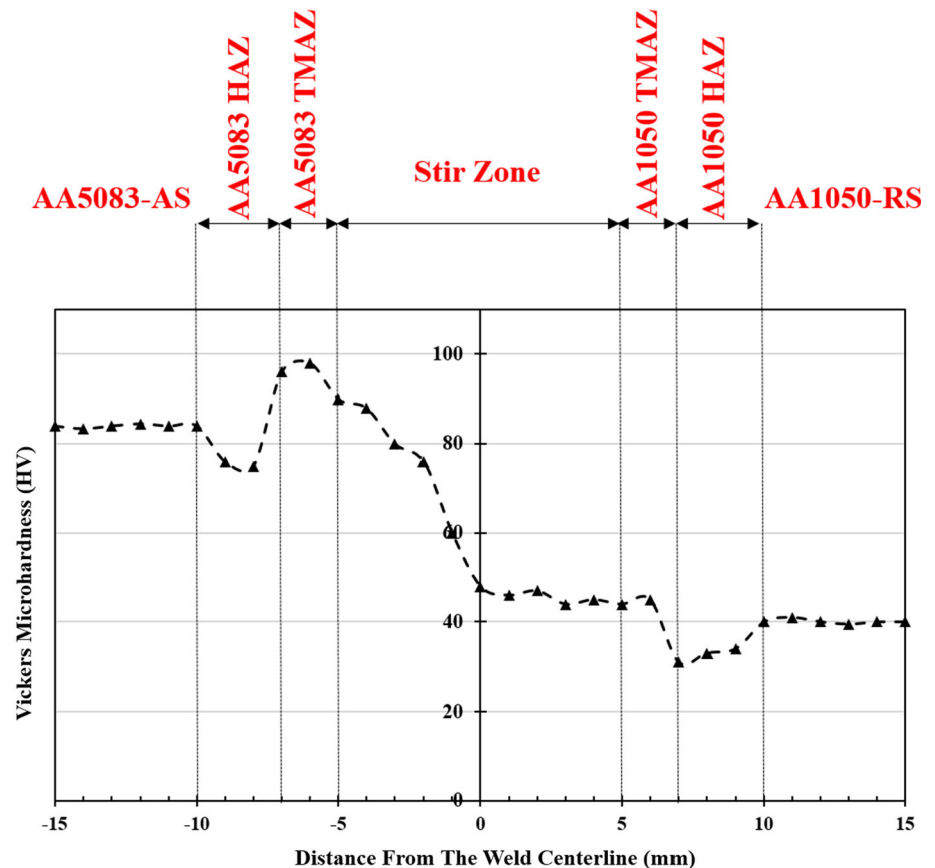
the shoulder and the top surface of the base metals during the process. Similar SZ morphologies have been reported in earlier studies conducted on the FSW of aluminum and its alloys [18–20].

One can easily notice the patent transitions between the base metals and the nugget on both AA1050 and AA5083 alloy sides, as shown in Figs. 3b, e. On AA1050 side (RS, Fig. 3b), a combination of elongated deformed and recrystallized grains can be recognized in the HAZ. In a similar manner, the identification of HAZ can be realized by noticing how grain sizes and shapes alter between the nugget and base metal on the AA5083 side (AS, Fig. 3e). The nugget zone shows a very fine recrystallized microstructure on its both sides, considering Fig. 3c, d. Moreover, the finer microstructure of AA5083 in the nugget zone compared to AA1050 helps the discrimination of interfacial regions. In fact, such a grain size variation was ascribed to a type of material response that resembles hot deformation conditions and particularly restoration mechanisms [23, 24].

FESEM imaging and EDS analysis of dissimilar FSW joint were taken (Fig. 4) to shed light on the distribution of second-phase particles in the base metal (AA5083) and the nugget zone. Second-phase particles present in the nugget zone are of much smaller average sizes when compared to that of the base metal. This has been attributed to the breakdown of initial second-phase particles by the action of threaded pin during the FSW processes [25].

Mechanical characterization

Hardness values were measured along the line at the center part of the cross section to establish the hardness profile shown in Fig. 5. Evidently, the dissimilar nature of joint has led to two distinct hardness profiles in the retreating (AA1050) and advancing (AA5083) sides. According to this Fig. 5, the hardness values of AA5083 TMAZ decrease sharply moving toward SZ and the average hardness of SZ is around 50 HV, which is lower than that of AA5083 base metal. Coexistence of fine and coarse second-phase particles in the aluminum matrix may be another

Figure 6 The typical tensile behavior of the base metals and dissimilar FSW joint at room temperature under strain rate of 1.67×10^{-4} s^{-1}.
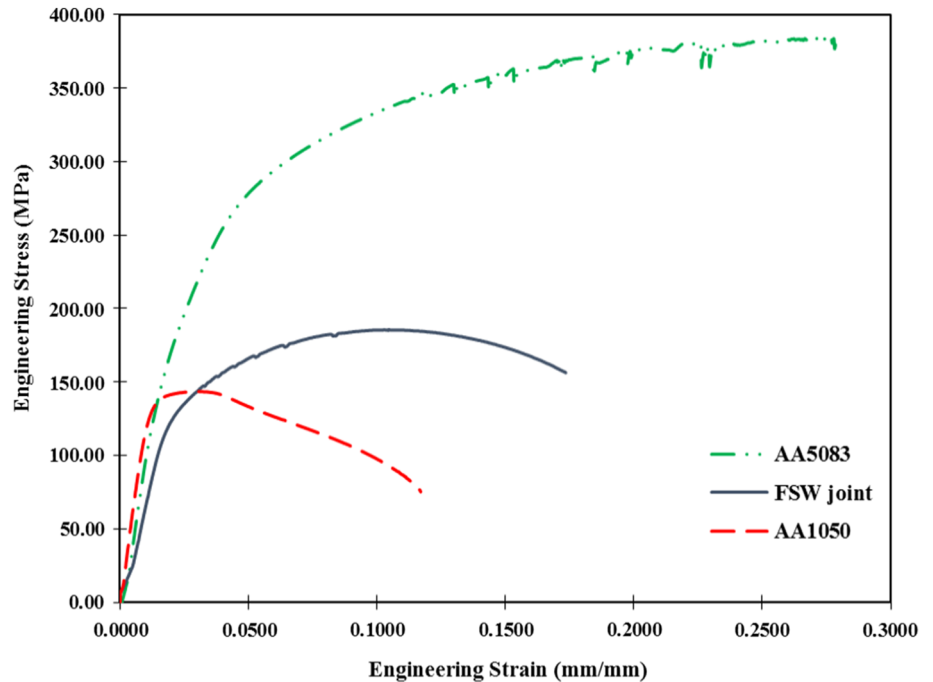
Table 2 Room temperature tensile properties of the base metals and dissimilar FSW joint in the cross-weld direction (three specimens were performed in each condition)

Sample	YS (MPa)	UTS (MPa)	Elongation (%)
AA5083	235	380	26.5
AA1050	118	132	11.2
FSW joint	135	178	17

factor that contributes to the fluctuation of hardness profile in SZ. In addition, the hardness values of AA1050 TMAZ decrease slightly toward AA1050 base metal. The somewhat low hardness values of this region may have originated from the dissolution and coarsening of grains in the aluminum microstructure or the lower dislocation density of this region that arose from the inherent thermomechanical nature of FSW [26, 27].

Furthermore, the lowest values of hardness in hardness profile belong to the region approximately 7–9 mm from the SZ center line at the AA1050 side or retreating side (AA1050 HAZ area). These low values can be due to the dissolution of second-phase particles and existence of somewhat larger grains. On the other hand, the relatively smaller hardness reduction of AA5083 HAZ area reveals that microstructural and metallurgical changes were less likely to happen in this region because such changes require higher temperatures [18, 21, 22]. It is also worth mentioning that in AA5083, top area is of higher hardness values when compared to the middle and bottom areas, which can be explained by the work hardening of AA5083 alloy. The tensile curves of base metals and FSW joint are all represented in Fig. 6, and the obtained mechanical properties are reported in Table 2. The ultimate tensile strength (UTS) and yield strength (YS) of the FSW joint sample are higher than

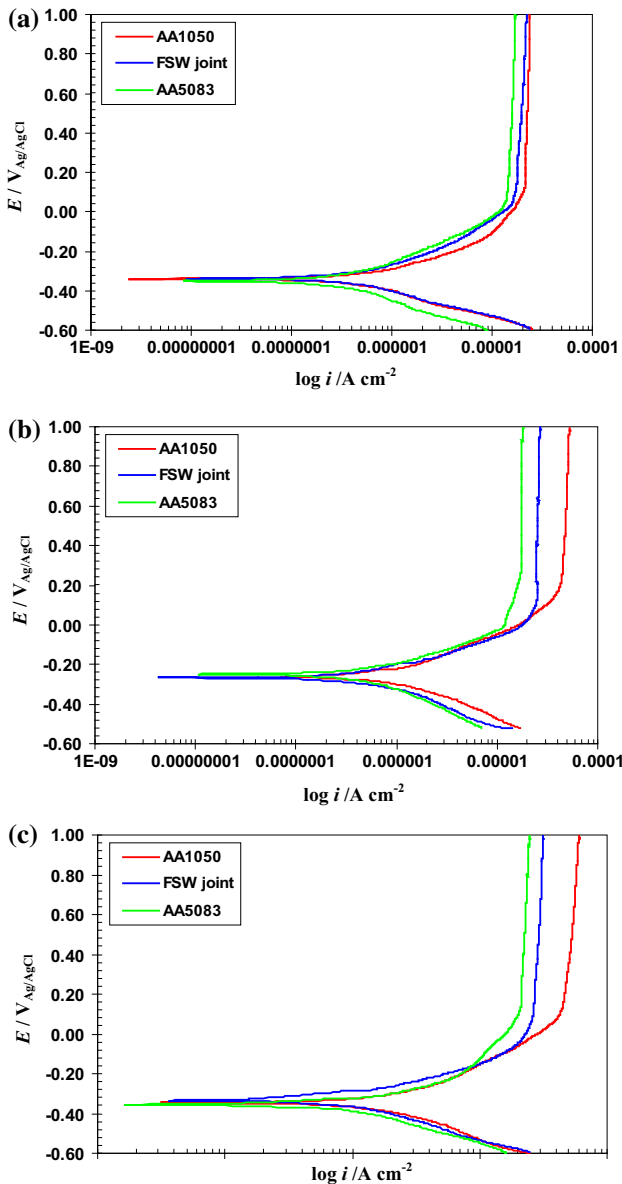**Figure 7** The macro-graph of fractured dissimilar FSW joint sample.
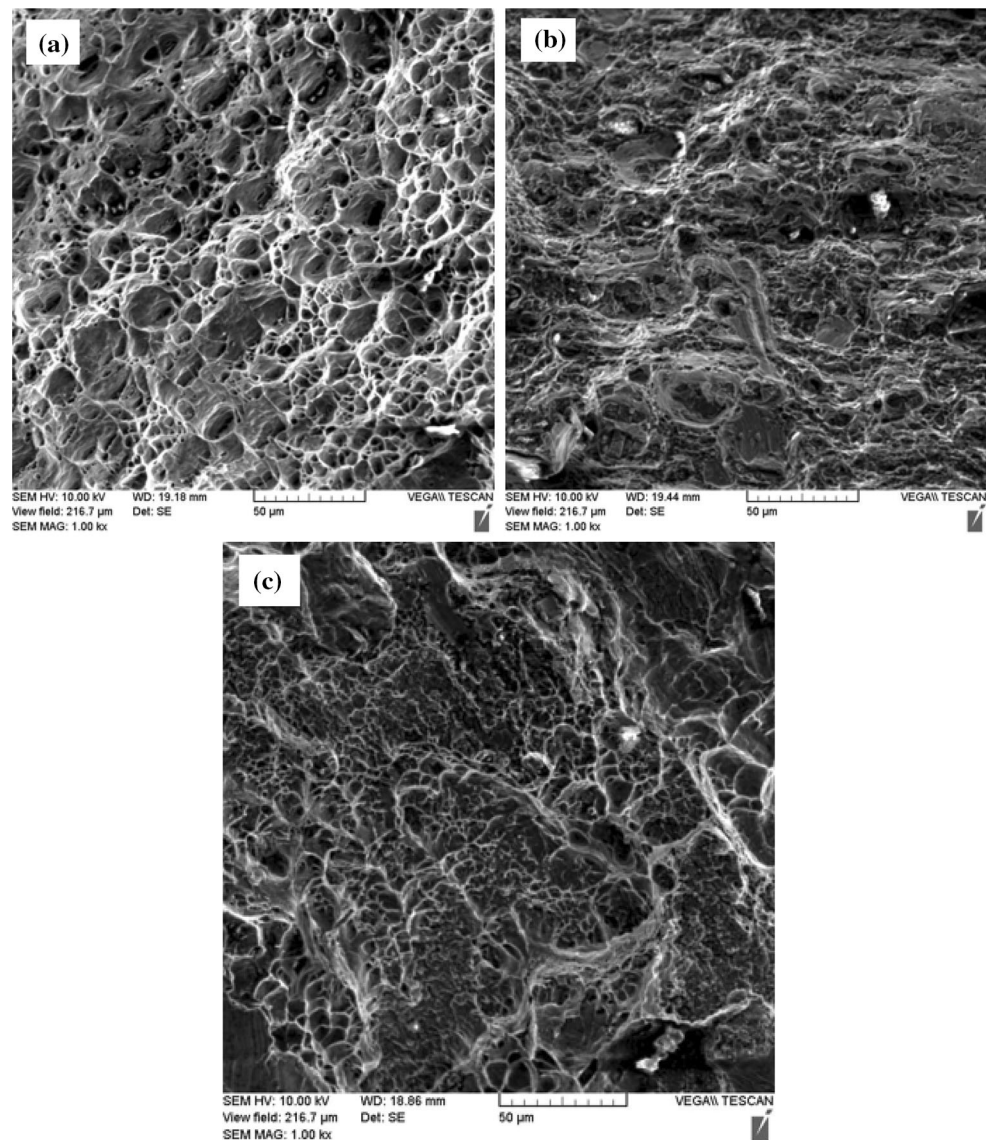
Figure 8 SEM fractographs of **a** AA1050 base metal, **b** AA5083 base metal and **c** dissimilar FSW joint.

those of the AA1050 base metal, yet lower than those of AA5083 base metal. Welding efficiency defined as the ratio of the strengths of welded region to base material can be calculated by UTS values [11, 14]. Since AA1050 alloy has the lower strength, its UTS value was used for this calculation and welding efficiency was found to be ~ 135%. The occurrence of fracture in the AA1050 side of the dissimilar FSW joint (Fig. 7) is in good agreement with the location of minimum hardness (Fig. 5). Here, the best-case scenario is that the fracture must be seen either at the weaker parent metal (AA1050) or at the HAZ adjacent to AA1050 side, considering its lower strength compared to SZ. This state can be ensured by a weld

region that is almost defect-free or when the stress concentration caused by defects could not surpass the strength of SZ [6, 8]. The fracture surfaces of tensile specimens were examined by FESEM in order to gain more insight on the mode of fracture. Figure 8 shows the fracture surfaces of the base metals (AA1050 and AA5083) and the dissimilar FSW joint. One can easily notice that various dimples cover all of these fracture surfaces, attesting to their ductile nature [28, 29]. Although the fracture surface of dissimilar FSW joint is covered by mostly fine shallow dimples, a relatively low portion of this surface shows sporadic small particles detectable in some large dimples and tearing edges. While the fracture surfaces of base

Figure 9 Potentiodynamic polarization curves for different regions in the studied solutions at **a** pH = 7; **b** pH = 8.1; and **c** pH = 8.9 after 2 h of immersion.

Table 3 Estimated corrosion current densities and corrosion potentials based on potentiodynamic polarization measurements

pH	Sample	$i_{corr}/\mu A\ cm^{-2}$	$E_{corr}/V_{Ag/AgCl}$
7.0	AA1050	0.17	− 0.334
	FSW joint	0.15	− 0.349
	AA5083	0.12	− 0.352
8.1	AA1050	0.19	− 0.254
	FSW joint	0.16	− 0.557
	AA5083	0.14	− 0.242
8.9	AA1050	0.25	− 0.365
	FSW joint	0.19	− 0.351
	AA5083	0.16	− 0.381

According to Fig. 9, all three regions have comparable corrosion potentials at each pH level. More importantly, SZ possesses a passive current density that is between those of AA1050 and AA5083 parent alloys. In addition, the main electrochemical parameters that can be drawn from PDP measurements are given in Table 3. As can be seen, the corrosion current density of FSW joint is between those of parent materials at all pH levels considered in this study. Although the same trend can be seen for corrosion potentials at pH 7.0 and 8.9, the corrosion potential of FSW joint is lower than those of parent materials at pH 8.1. This means that the passive layer on FSW joint might be slightly weaker at this particular pH level. The passivation behavior of SZ may be explained by the grain refinement of FSW process. In fact, the materials experience severe plastic deformation, which eventually leads to the development of fine and equiaxed recrystallized grains. In line with that, it has been reported that grain refinement of Al/B_4C/SiC hybrid composite occurs with increasing the number of accumulative roll bonding (ARB) cycles, which consequently leads to the formation of strong passive films [30]. In addition, Abdulstaar et al. [31] found that ultra-fine-grained (UFG) AA1050 that was obtained from the severe plastic deformation induced by rotary swaging exhibited a higher corrosion resistance compared to its coarse-grained (CG) counterpart. They reported that the high density of grain boundaries and dislocations gave rise to the easier formation of passive films in UFG AA1050, which was further explained by the role of internal residual stresses in making the passive film more stable and integral compared to its CG counterpart [30, 31].

metals are covered with inhomogeneous dimples containing larger second-phase particles, the fracture surface of joint exhibits finer second-phase particles.

Electrochemical behavior

The results of potentiodynamic polarization (PDP) acquired from the three regions of AA1050, SZ in FSW joint and AA5083 in the aforementioned borate buffer solutions are shown in Fig. 9. As can be seen, all of them exhibit a typical passive behavior.
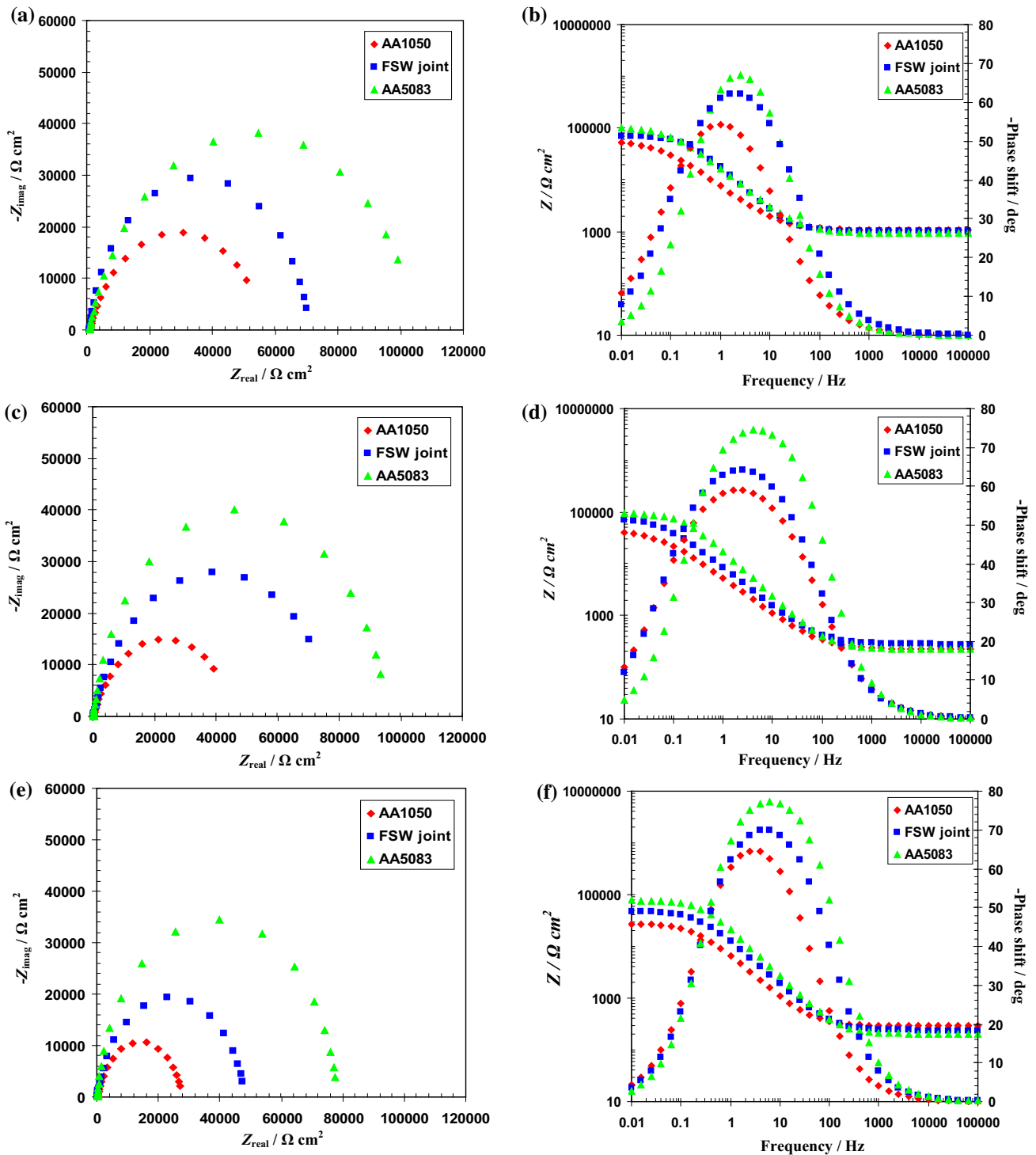
Figure 10 Kramers–Kronig transformations of the impedance diagrams obtained for FSW joint region in the studied solutions at **a** pH = 7; **b** pH = 8.1; and **c** pH = 8.9 after 2 h of immersion.
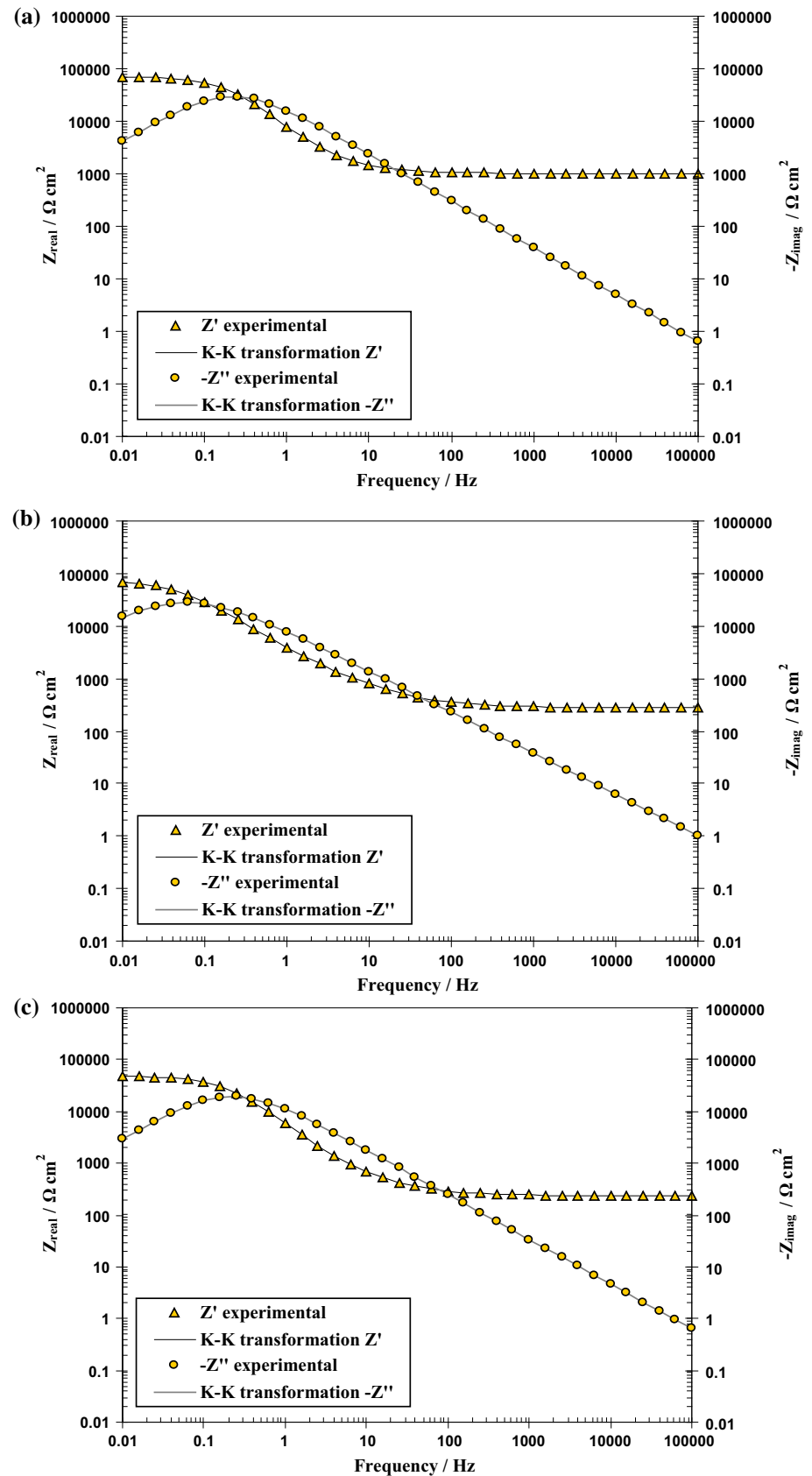
Figure 11 Nyquist (left) and Bode plots (right) of different regions after 2 h of immersion in borate buffer solutions. **a** pH = 7; **b** pH = 8.1; and **c** pH = 8.9.

It was also reported that phenomena such as the formation of various grain microstructures and dynamic recrystallization of grains occurring during the heat treatment and FSW of 5xxx alloy series led to their different corrosion susceptibilities in sub-regions of the jointed zone [32, 33]. Hariri et al. [33] investigated the influence of FSW parameters on passivation properties of AA5052. They reported that
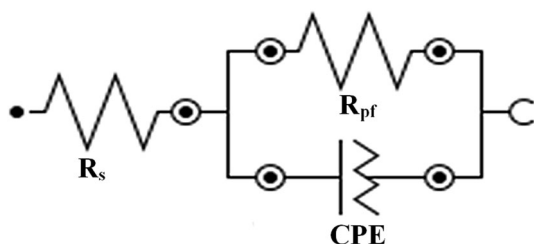
Figure 12 Equivalent circuit (EC) used for the modeling of experimental EIS data.

under optimum welding conditions, passivation behavior of the FSW-processed alloy improves. They have claimed that the fine-grained structure of SZ in these FSW-processed aluminum alloys facilitates the nucleation and growth of passive films. EIS was also employed to investigate the relative stability of the passive films formed on the surfaces of parent alloys and SZ in the above-mentioned borate buffer solutions. EIS measurements were recorded after 2 h of passive film formation at OCP.

It would be advisable to check whether raw EIS data are reliable and free from unwanted errors. To this end, the linear system theory (LST) has set certain constraints (i.e., causality, linearity and stability) that must be met by the electrochemical system under investigation [34]. Kramers–Kronig (K–K) transformations have been successfully used for such purposes, in which one transforms the real axis into the imaginary axis and vice versa and finally compares the transformed quantities with its respective experimental data [35]. As an example, Fig. 10 shows such comparisons between the obtained experimental data of SZ and its corresponding K–K transforms in test solutions. Similar comparisons were made for other regions as well (not shown here), and the reliability of all experimental data was ensured.

Figure 11 shows the impedance spectra obtained in different test solutions, presented in both Nyquist and Bode magnitude/phase plots. As can be seen in Fig. 11, only one time constant is needed to describe each of these impedance spectra. Moreover, all three regions show similar passivation mechanism. Since the ideal case would be to have phase angle values that approach 90°, a deviation from the ideal capacitive behavior is expected to exist in each of these responses. Accordingly, use of a constant phase element (CPE) seems necessary to justify this deviation from ideality. Various factors such as surface heterogeneity and roughness, impurities, dislocations, grain boundaries, adsorption of species and the formation of porous layers are thought to be responsible for these deviations [35]. In theory, the impedance of CPEs can be expressed as what follows [34]:

$$Z_{CPE} = \frac{1}{Q(j\omega)^{\alpha}} \tag{1}$$

where Q, ω, j and α are the CPE constant, the angular frequency in rad/s, the imaginary number ($j^2 = 1$) and the CPE exponent, respectively. Here, the value of α determines what can be represented by a CPE: a resistance ($\alpha = 0$, $Z_0 = R$), a capacitance ($\alpha = 1$, $Z_0 = C$) or a Warburg impedance ($\alpha = 0.5$, $Z_0 = W$).

For all fitting purposes, the EC shown in Fig. 12 would be appropriately used, where R_S and R_P represent solution resistance and passive film resistance, respectively. Furthermore, the passive film capacitance (C_P) can be extracted by knowing the CPE constant, CPE exponent and polarization or passive film resistance, such as given below [16, 36, 37]:

$$C_p = (Q)^{\frac{1}{\alpha}} \left(R_p^{\frac{(1-\alpha)}{\alpha}} \right) \tag{2}$$

Table 4 Electrical parameters obtained by fitting the experimental results of EIS for different samples after passive film formation in different pH values

pH	Sample	R_P/kΩ cm^2	$(Q/10^{-6})$/Ω^{-1} cm^{-2} S^n	n	C_p/μF cm^{-2}	R_s/kΩ cm^2
7.0	AA1050	56.192	33.125	0.757	46.664	1.068
	FSW joint	69.760	13.375	0.803	14.671	1.011
	AA5083	104.320	9.9530	0.891	10.560	0.921
8.1	AA1050	46.336	47.9687	0.733	29.470	0.220
	FSW joint	79.361	26.875	0.782	14.367	0.276
	AA5083	95.361	11.000	0.889	7.985	0.226
8.9	AA1050	27.520	30.468	0.841	64.166	0.288
	FSW joint	48.0642	15.109	0.864	33.193	0.230
	AA5083	78.083	8.281	0.923	11.065	0.205

Table 4 lists all of these equivalent electrical parameters for the three regions of interest at each pH level. As can be seen, both the passivation resistance and capacitance of SZ are between those obtained for parent alloys. It is important to notice that EIS results corroborate the PDP results discussed above. Overall, FSW leads to a joint region that is not necessarily superior to its parent alloys, but rather exhibiting middling properties with regard to either mechanical or electrochemical aspects.

Conclusions

Metallurgical structure, mechanical properties and electrochemical behavior of dissimilar FSW joints between AA5083 and AA1050 alloys were thoroughly investigated. In what follows, it is attempted to summarize the main findings of this research briefly:

1. FSW led to substantial microstructural evolution, which was followed by the appearance of four distinct zones of different characteristics, namely nugget zone (NZ), thermomechanically affected zone (TMAZ), heat-affected zone (HAZ) and base metals (BM).
2. Joining of AA5083 and AA1050 alloys by FSW resulted in a weld nugget zone that mostly contains fine and equiaxed grains.
3. The fracture of studied dissimilar FSW joint took place in its weaker AA1050 side, which accorded well with the lowest seen hardness values on microhardness plot. The tensile strength of the FSW joint (178 MPa) was found to be much higher than that of AA1050 base metal (132 MPa), yet lower than that of AA5083 base metal (380 MPa).
4. Both PDP and EIS result indicated that the studied dissimilar FSW joint leads to a region that has an average passivation behavior between those of AA1050 and AA5083 parent alloys.

Acknowledgements

References

[1] Pérez-Bergquist SJ, Gray GT, Cerreta EK, Trujillo CP, Pérez-Bergquist A (2011) The dynamic and quasi-static mechanical response of three aluminum armor alloys: 5059, 5083 and 7039. Mater Sci Eng, A 528:8733–8741

[2] Katsas S, Nikolaou J, Papadimitriou G (2006) Microstructural changes accompanying repair welding in 5xxx aluminium alloys and their effect on the mechanical properties. Mater Des 27:968–975

[3] Fattah-alhosseini A, Naseri M, Alemi MH (2017) Effect of particles content on microstructure, mechanical properties, and electrochemical behavior of aluminum-based hybrid composite processed by accumulative roll bonding process. Metall Mater Trans A 48(3):1343–1354

[4] Thomas WM, Nicholas ED, Needham JC, Murch MG, Temple-Smith P, Dawes CJ (1991) International patent application PCT/GB92/02203 and GB Patent Application 9125978.8, UK Patent Office, London, December 6, 1991

[5] Dawes CJ, Thomas WM (1995) TWI Bulletin 6, November/December, 1995, 124

[6] Lee WB, Yeon YM, Jung SB (2003) The improvement of mechanical properties of friction-stir-welded A356 Al alloy. Mater Sci Eng, A 355:154–159

[7] Nandan R, Roy GG, Lienert TJ, Debroy T (2007) Three-dimensional heat and material flow during friction stir welding of mild steel. Acta Mater 55:883–895

[8] Fattah-alhosseini A, Taheri AH (2015) Effect of friction stir welding on corrosion behavior of pure copper in 3.5 wt% NaCl solution. J Manuf Process 20:98–103

[9] Sato YS, Kokava H (2001) Distribution of tensile property and microstructure in friction stir weld of 6063 aluminum. Metall Mater Trans A 32:3023–3031

[10] Elangovan K, Balasubramanian V (2008) Influences of tool pin profile and tool shoulder diameter on the formation of friction stir processing zone in AA6061 aluminum alloy. Mater Des 29:362–373

[11] Babu S, Elangovan K, Balasubramanian V, Balasubramanian M (2009) Optimizing friction stir welding parameters to maximize tensile strength of AA2219 aluminum alloy joints. Met Mater Int 15:321–330

[12] Zhang Z, Xiao BL, Ma ZY (2012) Effect of welding parameters on microstructure and mechanical properties of

friction stir welded 2219Al-T6 joints. J Mater Sci 47:4075–4086. https://doi.org/10.1007/s10853-012-6261-1

[13] Liu HJ, Zhou L, Liu QW (2010) Microstructural characteristics and mechanical properties of friction stir welded joints of Ti–6Al–4V titanium alloy. Mater Des 31:1650–1655

[14] Zhou L, Liu HJ, Liu QW (2010) Effect of rotation speed on microstructure and mechanical properties of Ti–6Al–4V friction stir welded joints. Mater Des 31:2631–2636

[15] Zhou L, Liu HJ, Liu P, Liu QW (2009) The stir zone microstructure and its formation mechanism in Ti–6Al–4V friction stir welds. Scr Mater 61:596–599

[16] Shen C, Zhang J, Ge J (2011) Microstructures and electrochemical behaviors of the friction stir welding dissimilar weld. J Environ Sci 23:S32–S35

[17] Park SK, Hong ST, Park JH, Park KY, Kwon YJ, Son HJ (2010) Effect of material locations on properties of friction stir welding joints of dissimilar aluminium alloys. Sci Technol Weld Join 15:331–336

[18] Liu XC, Sun YF, Fujii H (2017) Clarification of microstructure evolution of aluminum during friction stir welding using liquid CO_2 rapid cooling. Mater Des 129:151–163

[19] Cabibbo M, Forcellese A, Simoncini M, Pieralisi M, Ciccarelli D (2016) Effect of welding motion and pre-/post-annealing of friction stir welded AA5754 joints. Mater Des 93:146–159

[20] Aval HJ (2015) Microstructure and residual stress distributions in friction stir welding of dissimilar aluminium alloys. Mater Des 87:405–413

[21] Carter H, Stanisaw D, Marek B (2008) A model of material flow during friction stir welding. Mater Charact 59:1206–1214

[22] Hu ZL, Wang XS, Yuan SJ (2012) Quantitative investigation of the tensile plastic deformation characteristic and microstructure for friction stir welded 2024 aluminum alloy. Mater Charact 73:114–123

[23] Amra M, Ranjbar Kh, Dehmolaei R (2015) Mechanical properties and corrosion behavior of CeO_2 and SiC incorporated Al5083 alloy surface composites. J Mater Eng Perform 24(8):3169–3179

[24] Alvand M, Naseri M, Borhani E, Abdollah-Pour H (2017) Nano/ultrafine grained AA2024 alloy processed by accumulative roll bonding: a study of microstructure, deformation texture and mechanical properties. J Alloy Compd 712:517–525

[25] Amra M, Ranjbar Kh, Hosseini SA (2018) Microstructure and wear performance of Al5083/CeO_2/SiC mono and hybrid surface composites fabricated by friction stir processing. Trans Nonferrous Metals Soc China 28(5):866–878

[26] Chowdhury SM, Chen DL, Bhole SD, Cao X (2010) Tensile properties of a friction stir welded magnesium alloy: effect of pin tool thread orientation and weld pitch. Mater Sci Eng A 527:6064–6075

[27] Ueji R, Fujii H, Cui L, Nishioka A, Kunishige K, Nogi K (2006) Friction stir welding of ultrafine grained plain low-carbon steel formed by the martensite process. Mater Sci Eng A 423:324–330

[28] Gashti SO, Fattah-alhosseini A, Mazaheri Y, Keshavarz MK (2016) Microstructure, mechanical properties and electrochemical behavior of AA1050 processed by accumulative roll bonding (ARB). J Alloys Compd 688:44–55

[29] Naseri M, Hassani A, Tajally M (2015) An alternative method for manufacturing Al/B_4C/SiC hybrid composite strips by cross accumulative roll bonding (CARB) process. Ceram Int 41(10, Part A):13461–13469

[30] Fattah-alhosseini A, Naseri M, Alemi MH (2016) Corrosion behavior assessment of finely dispersed and highly uniform Al/B_4C/SiC hybrid composite fabricated via accumulative roll bonding process. J Manuf Process 22:120–126

[31] Abdulstaar M, Mhaede M, Wagner L, Wollmann M (2014) Corrosion behaviour of Al 1050 severely deformed by rotary swaging. Mater Des 57(2014):325–329

[32] Davoodi A, Esfahani Z, Sarvghad M (2016) Microstructure and corrosion characterisation of the interfacial region in dissimilar friction stir welded AA5083 to AA7023. Corros Sci 107:133–144

[33] Hariri MB, Shiri SG, Yaghoubinezhad Y, Rahvard MM (2013) The optimum combination of tool rotation rate and traveling speed for obtaining the preferable corrosion behavior and mechanical properties of friction stir welded AA5052 aluminum alloy. Mater Des 50:620–634

[34] Macdonald JR, Barsoukov E (2005) Impedance spectroscopy: theory, experimentand applications. Wiley, Hoboken

[35] Escrivà-Cerdán C, Blasco-Tamarit E, García-García D, García-Antón J, Akid R, Walton J (2013) Effect of temperature on passive film formation of UNS N08031 Cr–Ni alloy in phosphoric acid contaminated with different aggressive anions. Electrochim Acta 111:552–561

[36] Vafaeian S, Fattah-alhosseini A, Keshavarz MK, Mazaheri Y (2016) The influence of cyclic voltammetry passivation on the electrochemical behavior of fine and coarse-grained AISI, 430 ferritic stainless steel in an alkaline solution. J Alloys Compd 677:42–51

[37] Fattah-alhosseini A, Gashti SO (2015) Corrosion behavior of ultra-fine grained 1050 aluminum alloy fabricated by ARB process in a buffer borate solution. J Mater Eng Perform 24(2015):3386–3393